Catalysis Today 159 (2011) 47–54

Contents lists available at ScienceDirect

Catalysis Today

journal homepage: www.elsevier.com/locate/cattod

Quaternary mixture designs applied to the development of multi-element oxygen electrocatalysts based on the $Ln_{0.58}Sr_{0.4}Fe_{0.8}Co_{0.2}O_{3-\delta}$ system ($Ln = La_{1-x-y-z}Pr_xSm_yBa_z$): Predictive modeling approaches

José M. Serra*, Vicente B. Vert

Instituto de Tecnología Química (Universidad Politécnica de Valencia – Consejo Superior de Investigaciones Científicas),
Av. Los Naranjos, s/n, Building 6C, Campus UPV, 46022 Valencia, Spain

ARTICLE INFO

Article history:
Available online 29 July 2010

Keywords:
SOFC
Cathodes
Data mining
Electrochemical impedance spectroscopy
Mixture design
Fuel cell
Perovskite
Predictive modeling

ABSTRACT

The experimental data generated through the optimization of oxygen electrocatalysts based on the perovskite $Ln_{0.58}Sr_{0.4}Fe_{0.8}Co_{0.2}O_{3-\delta}$ system ($Ln = La_{1-x-y-z}Pr_xSm_yBa_z$) have been modeled following different approaches. The main application of these catalysts is as fuel cell (SOFC) cathodes and activation layers on oxygen-transport membranes. Among the different La, Pr and Sm combinations, those containing at a time Sm–La–Ba or alternatively Pr–La–Ba show the lowest polarization resistance values. Within the same substitution degree, Pr–Ba-based compositions have lower electrode resistance than samarium-based ones. The experimental datasets available for the series of materials can be divided into: composition data, structural data (X-ray diffraction patterns), and electrochemical characterization data (electrochemical impedance spectra). Electrochemical characterization was performed for each electrode composition as a function of the operating temperature and oxygen partial pressure. Different ways of reducing the dimensionality of the spectral descriptors (XRD patterns and impedance spectroscopy) were applied based on knowledge-guided and unsupervised approaches. Different material descriptors were studied as input variables in the modeling of the electrochemical properties.

1. Introduction

High-temperature oxygen activation catalysts/electrocatalysts are multifunctional materials generally made of multimetallic crystalline mixed oxides with well-adjusted properties, i.e., solid state oxygen-ion and electronic conduction, adequate layer porosity, catalytic activity for oxygen reduction and oxygen-ion incorporation into the oxide bulk. Perovskite oxides based on manganese, iron and cobalt [1] have shown promising electrochemical activity for oxygen activation used in classical solid oxide fuel cell (SOFC) configurations [2–4]. The perovskite structure [5] presents a huge potential for the simultaneous optimization of the catalytic properties [6] since this structure can accommodate in the lattice a large number of non-precious metals in different oxidation states. Moreover, the variation of the operating temperature above 400 °C and oxygen partial pressure results in the formation of new oxygen vacancies, which leads to structural changes (chemical expansion and evolution of the perovskite symmetry) and changes in the catalytic properties, which are related to changes of the redox state of surface cations and the increase in the population of surface vacancies (adsorption sites). The perovskite structure appears as an ideal catalytic piece for the systematic study of the lattice composition since this structure allows packing together different active metals and promoters in the crystal bulk and surface.

Parallel physico-chemical characterization of libraries of materials allows identifying potential high-performing candidates for a given property and generally they should be confirmed and optimized in a further experimental step. Several spectroscopic techniques have been parallelized for the screening of solid materials as for instance, XRD systems [7,8], acidity determination by TPD-NH_3 [9] and FTIR-pyridine adsorption [10], thermo gravimetrical techniques [11], photoluminescence [12], Raman [13], impedance spectroscopy [14], EXAFS [15], etc. However, it is still a challenge the automated processing of the spectral data, which entails validation, fitting to knowledge-based [16] or empirical model and quantitative reporting [17].

Different machine learning (ML) methods have been applied successfully to quantitative structure–property relationship (QSPR) modeling in materials science as for instance in ferromagnetism [18], bulk mechanical properties [19] and catalytic behavior [24,20,21] modeling of large libraries of solid materials produced by HTE techniques. Among the different modeling techniques it can be highlighted the use of this field of artificial neural networks [22] and support vector machines [23]. The better modeling perfor-

---

* Corresponding author. Tel.: +34 963879448; fax: +34 963877809.
E-mail address: jsalfaro@itq.upv.es (J.M. Serra).

0920-5861/$ – see front matter © 2010 Elsevier B.V. All rights reserved.
doi:10.1016/j.cattod.2010.06.019

mance of ML methods with respect to conventional methods is due to several reasons, i.e., the complexity of each specific spectroscopy data and the associated fitting to theoretical data, the diversity among samples, deviations during the library preparation (compositional, structural, etc.), variation in the sample conditioning for the characterization process, etc.

In the present case, two different spectroscopic techniques have been applied to the characterization of a well-defined library of crystalline materials. After sample preparation, the powders were characterized by X-ray diffraction. XRD data contains information about phase purity, perovskite phase symmetry, unit cell dimensions and crystallite size. For the given application of oxygen activation, electrochemical impedance spectroscopy (EIS) permits obtaining a rather complete picture of the performance in the range from 450 °C to 650 °C of the materials as catalytic layer on a pure ionic conductor electrolyte. EIS spectra can be fitted to a phenomenological model, which includes the different steps or single mechanism contributing to the operation of the catalytic layer. A major drawback of this technique is the complexity of data modeling and the tremendous influence of experimental factors on the measurements, which leads to the occurrence of severe artifacts. This is especially critical when the total measured impedance is small, i.e., when the electrocatalytic activity is good.

This work presents the data treatment and dimensional reduction of both spectroscopic datasets. The different classes of descriptors are employed to build relationships (QSPR/QSAR). These models can be integrated in the optimization/discovery campaigns [24] by using fast characterization of libraries of catalysts, as multivariate spectral descriptors for catalytic QSPR modeling. This approach can find application in the field of heterogeneous combinatorial catalysis [25–27] and electrocatalysis [28]. Moreover, QSPR models could be used for assisting the design of new libraries as well as for extraction of rules and relationships, gaining knowledge about (electro-) catalysis. This approach can be of special interest when the experimental evaluation of the catalytic behavior is complex and time-consuming, as for instance for catalyst deactivation studies or dual-chamber testing of multilayered fuel cells.

2. Experimental

Experimental data was drawn from a previous optimization study [29] of oxygen activation catalysts/electrocatalysts based on the system $A_{0.58}Sr_{0.4}Fe_{0.8}Co_{0.2}O_{3-\delta}$. The catalysts were crystalline and their composition was varied following a quaternary mixture design. Specifically, only the A position of the perovskite structure was varied and the stoichiometry of the resting elements, i.e., Sr, Fe and Co, was kept constant. Up to four different elements were incorporated simultaneously in the A position. The mixture experimental design is depicted in Fig. 1. The elements (La, Pr, Sm and Ba) were chosen considering their potential (electro) catalytic properties [30] (redox and basic sites) and the fact that they could accommodate properly in the A position due to their ionic radius and oxidation state.

The multimetallic crystalline solids corresponding to the mixture design were synthesized in parallel on a robotic system (Zinsser Sophas-Cat®) following a citrate-complexation sol–gel route [31,32] and finally sintered at 1000 °C for 3 h in quartz vials. The obtained materials were characterized on 4 × 6 arrays by XRD using a Phillips X Pert diffractometer employing CuK_α radiation and the scanned 2θ range was from 20° to 90°. The as-prepared powders were milled with 3YSZ balls in acetone for 15 h and screen-printing inks were prepared using terpineol and ethylcellulose. The electrodes were deposited by screen-printing on both sizes of gastight $Ce_{0.8}Gd_{0.2}O_{1.9}$ disk-shaped (16 mm OD) electrolytes. The electrochemical characterization was carried out by impedance spectroscopy (Solartron 1455A FRA) on two-point symmetrical configuration as a function of the operation temperature (450–650 °C) and oxygen partial pressure under gas flow (100 ml/min). EIS spectrum was recorded in the frequency range 0.01–10^5 Hz for each material and temperature and the polarization contributions were modeled as two contributions: (i) a high frequency arc related to transfer of active oxygen species to the electrolyte and electron-transfer process occurring at the current collector/electrode interface; and (ii) a low frequency arc (Gerischer element) ascribed to the solid state diffusion coupled to a chemical reaction on the electrode surface [33,34].

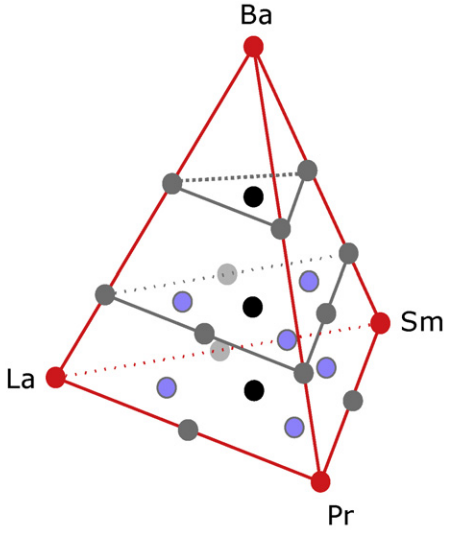

Fig. 1. Quaternary mixture design. The A position in the perovskite formula $A_{0.58}Sr_{0.4}Fe_{0.8}Co_{0.2}O_{3-\delta}$ is simultaneously occupied by four different elements.

Data mining (dimension reduction and modeling) was carried out using SPSS Clementine 9.0 Software. Neural network fitting was performed always using 80% of experimental data for training and the rest for validation to minimize over training issues as implemented in the neural network training tool of Clementine 9.0 [35]. Graphics were prepared using the software applications Mathcad 2000, Origin 8.1 and TeeChart (Steema Soft.) integrated in the hITeQ platform [36].

3. Methodology

The experimental data employed can be therefore divided into three groups: (i) compositional data: La, Pr, Sm and Ba lattice stoichiometry; (ii) XRD measurements; and (iii) electrochemical results. Firstly, the raw data has been pretreated to detect and eliminate error and blanks, and achieve descriptor fields totally comparable within the library samples. Errors and blanks needed typically the reprocessing of impedance spectroscopy data in order to obtain consistent polarization resistance and activation energy values. Then, spectral data has been treated to reduce the dimensionality and summarize the contained information into a reduced number of descriptors by using knowledge-based and unsupervised methods. Finally, different modeling techniques, i.e., linear regression and artificial neural networks, have been employed in order to build predictive models and find quantitative relationships among the different descriptors and diverse combinations of them. Table 1 summarizes the different data treatments and predictive models considered in this work, i.e., spectra analysis, dimension reduction and composition/structure/property relationships.

Table 1
Spectral data treatment and considered relationships among the different descriptors: synthesis, structural and electrochemical (activity).

Spectral data treatment	
Knowledge-based analysis	
XRD patterns (intensity, angle)	Structural descriptors Refinement: unit cell parameter Crystalline phase distribution: perovskite symmetries
Impedance data (real (Z'), imaginary (Z''), frequency, T)	Activity descriptors Parameters of the equivalent circuit elements(depressed arc (R-CPE) and Gerischer element) = R_p Activation energy
Unsupervised dimension reduction	
XRD patterns (intensity, angle)	Structural descriptors K-means clustering analysis Principal component analysis Kohonen networks[a]
Modeling & synthesis/structure/properties relationships	
Synthesis–structure relationships	
Input	Output
Synthesis descriptors (composition)	Unit cell parameter Crystalline phase distribution Principal components XRD patterns[a]
Synthesis–property relationships	
Input	Output
Synthesis descriptors (composition)	Polarization resistance Activation energy Impedance spectra[a]
Synthesis–property relationships	
Input	Output
Knowledge-based structural descriptors	Polarization resistance/activation energy
Unsupervised structural descriptors (principal components)	Polarization resistance/activation energy

[a] Proposed but not tackled in this work.

4. Analysis of XRD patterns and composition–structure relationships

4.1. Knowledge-based XRD analysis

The pseudo-cubic perovskite lattice parameter [37] was computed considering the squared root of the cell volume as calculated [38] for the XRD spectra recorded at room temperature. For a series of samples, minor impurities of a distinct perovskite symmetry phase (orthorhombic or hexagonal) from the cubic symmetry were detected. The abundance of those two impurities has been quantified for all samples. The orthorhombic abundance has been ranked in four levels (0–3) and the hexagonal only in 2 (0 and 2) and the value 0 means the absence of impurities, which is the most common case.

The knowledge-derived structural parameter could be predicted by considering the nominal composition (synthesis descriptor) of the each perovskite lattice. In principle, one could expect that the pseudo-cubic lattice parameter (a') is a linear combination of the ionic radii of the elements incorporated in the lattice (Vegard's law) and this is partially true for several compounds, as can be observed in Fig. 2a. This figure presents a parity plot of the experimental versus linear regression prediction of the lattice parameter. It seems that other non-linear factors are influencing the final unit cell dimension. Such factors are the occurrence of other perovskite symmetries, the alteration of the oxidation state of different cations, i.e., Fe, Co, Sm and Pr, and the subsequent variation of the oxygen vacancy concentration. Nevertheless, this non-linear behavior can be modeled very well using a relatively simple neural network (multilayer perceptron, Fig. 2b) achieving a prediction performance of 98.4%. The relative significance of the three ANN input variables is 0.53 for Ba%, 0.21 for La% and 0.13 for Pr% and these values are proportional to the corresponding ionic radii in 12-fold coordination, i.e., 1.61 Å (Ba^{2+}), 1.36 Å (La^{3+}) and 1.40 Å (Pr^{3+}). Fig. 3a shows a mapping simulated from best ANN (artificial neural network) model for the lattice parameter for Ba-free ternary section.

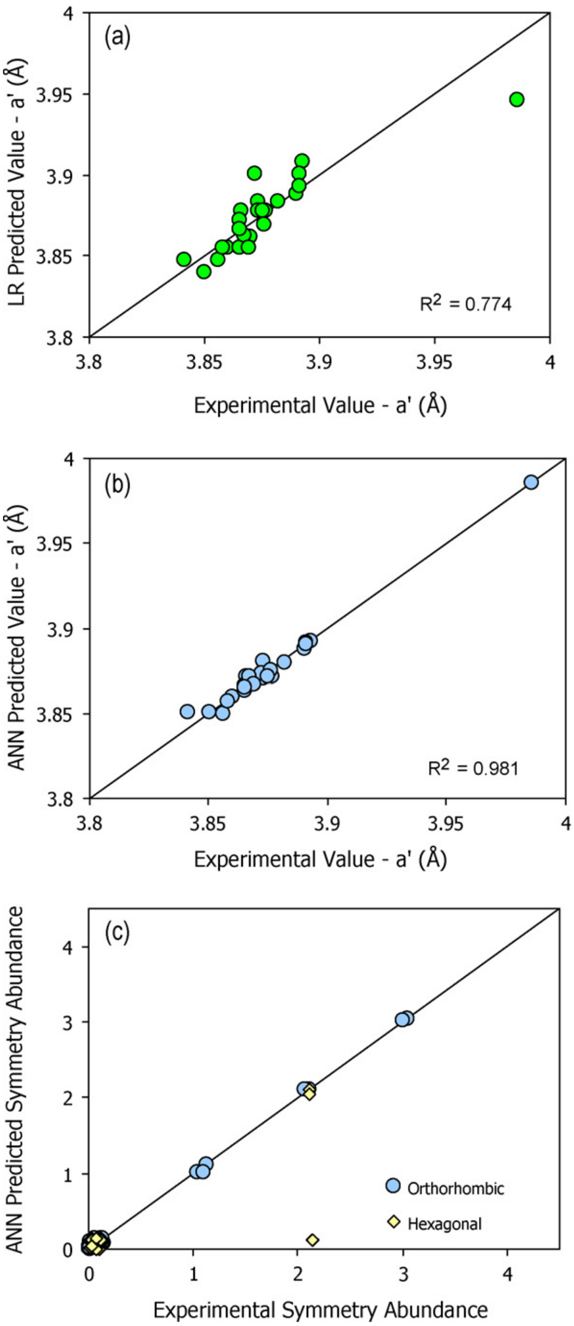

Fig. 2. Modeling of the knowledge-based structural parameters as a function of the material composition. Parity plots corresponding to: (a) linear regression of lattice parameter (the regression equation is $a' = \text{La}\ 0.02889 + \text{Pr}\ 0.01502 + \text{Ba}\ 0.1061 + 3.84$); (b) neural network modeling of lattice parameter (best ANN model has a topology including: 3 inputs, 3 neurons in a single hidden layer and a single output); and (c) neural network modeling of the occurrence of secondary phase symmetries (best ANN model has a topology including: 3 inputs, 3 neurons in a single hidden layer and a two outputs).

The abundance of orthorhombic and hexagonal symmetry has been modeled (Fig. 2c) utilizing a simple neural network and the prediction performances 98.0%. In this case, the relative input sig-

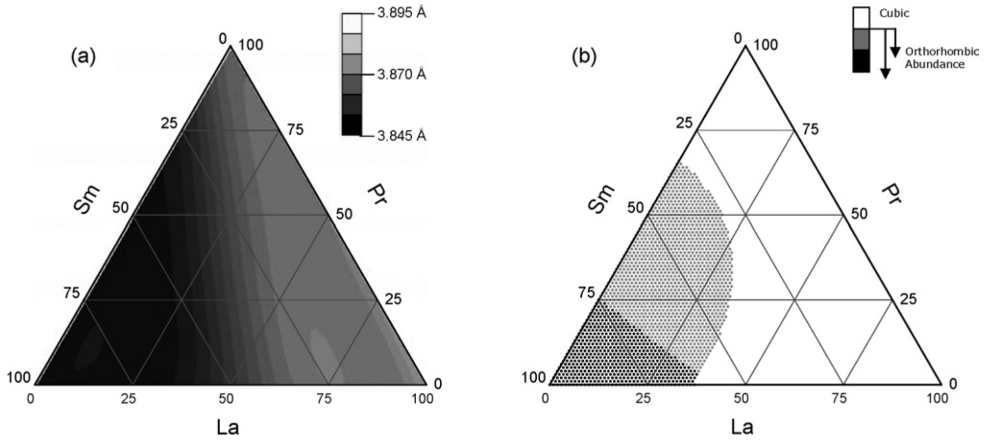

Fig. 3. Mapping simulated from best ANN models for (a) the lattice parameter and (b) the orthorhombic symmetry abundance in the Ba-free plane.

nificance follows the same order (Ba (0.60) > La (0.32) > Pr (0.26)) although the interpretation is more difficult. Namely, the presence of the orthorhombic symmetry is ascribed to high contents of Sm and Pr, and the effect of Sm content is complex since it is a linear combination of the other input parameter (Sm = 1 – Ba – La – Pr). Fig. 3b presents a clear picture of the influence of the elements in the final occurrence of the orthorhombic symmetry. This compositional mapping has been generated using the ANN model for the Ba-free

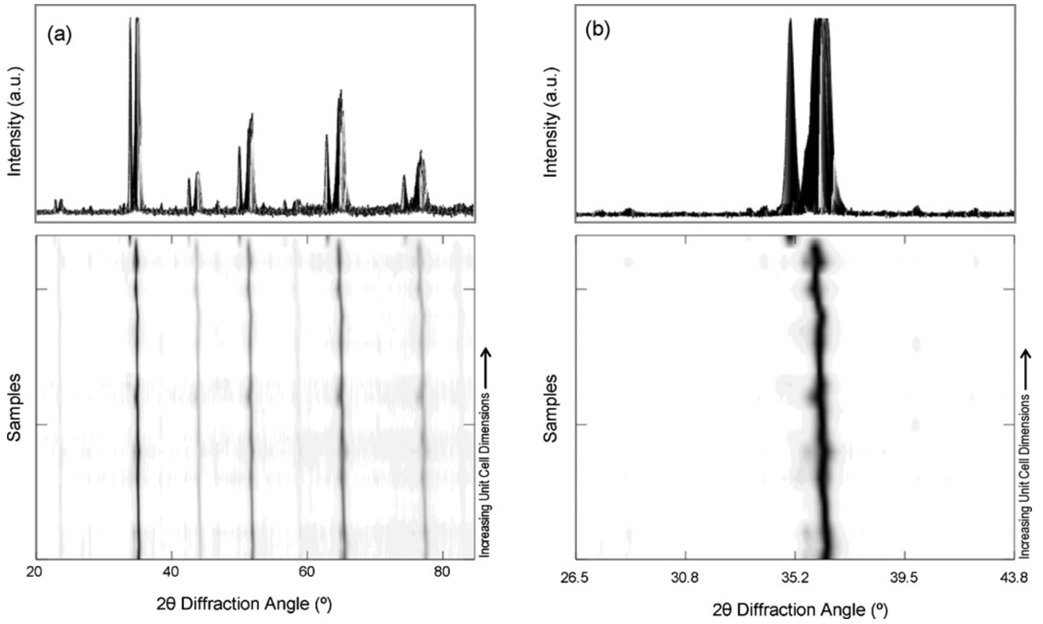

Fig. 4. X-ray diffraction data corresponding to samples screened in the quaternary mixture design. The samples are ordered by increasing unit cell parameter and the intensity has been normalized taking the most intense peak as reference: (a) whole diffraction angle range; and (b) selected angle range for the most intense diffraction peak.

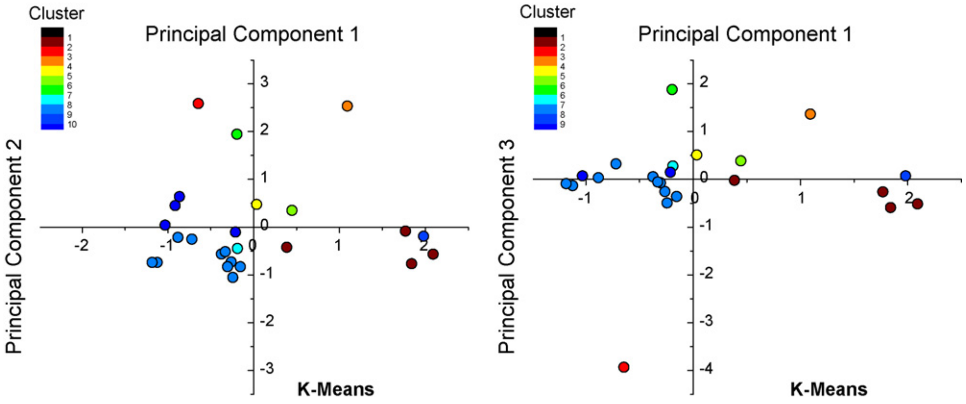

Fig. 5. K-Means clustering analysis represented in two-principal component projections (PC1–PC2 and PC1–PC3) for the classification of the whole material library. The corresponding percentage of variance for each principal component (PC#) is 20.1%, 12.96%, 10.4%, 6.8% and 5.9%.

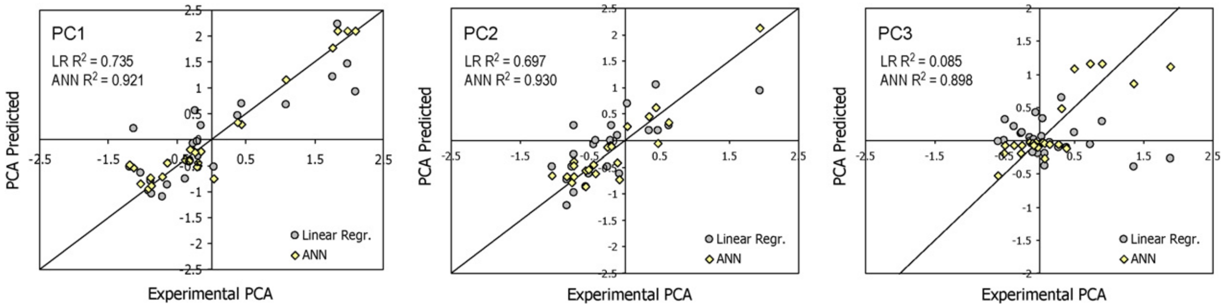

Fig. 6. Parity plots for the modeled PCA components using linear regression and ANNs. Best ANN model has a topology including 3 inputs, 3 neurons in a hidden layer and 3 outputs.

tetrahedron plane. The presence of the orthorhombic symmetry has been observed for compounds with considerable amounts of Sm (Sm^{3+} is the smallest A-site cation) and combinations with Pr. The case of hexagonal symmetry is simpler since it appears in compounds with high amounts of Ba, specifically Ba concentrations in the range 50–100% lead to the formation of the hexagonal phase.

4.2. Unsupervised analysis

XRD characterization data consist of arrays of more than 3000 values, which could be hardly processed by correlation methods when using them directly as input variables for predictive modeling (QSPR). For this reason as well as for reduction of experimental noise, a previous dimension reduction of the abundant raw data is needed. In the present case, XRD data will be analyzed and pro-

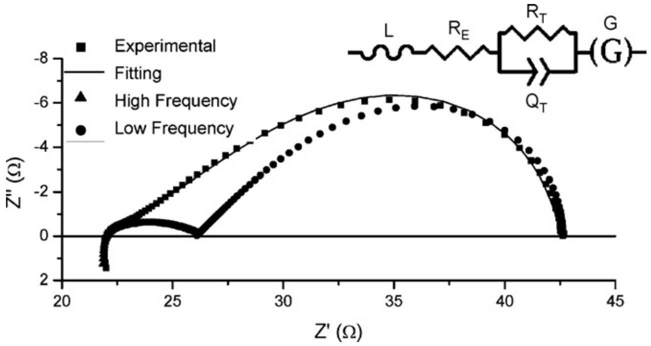

Fig. 7. Example of a Nyquist plot for raw EIS data recorded at 650 °C in air. Fitted data and separated electrode contributions obtained by the equivalent circuit model (inset) are also plotted.

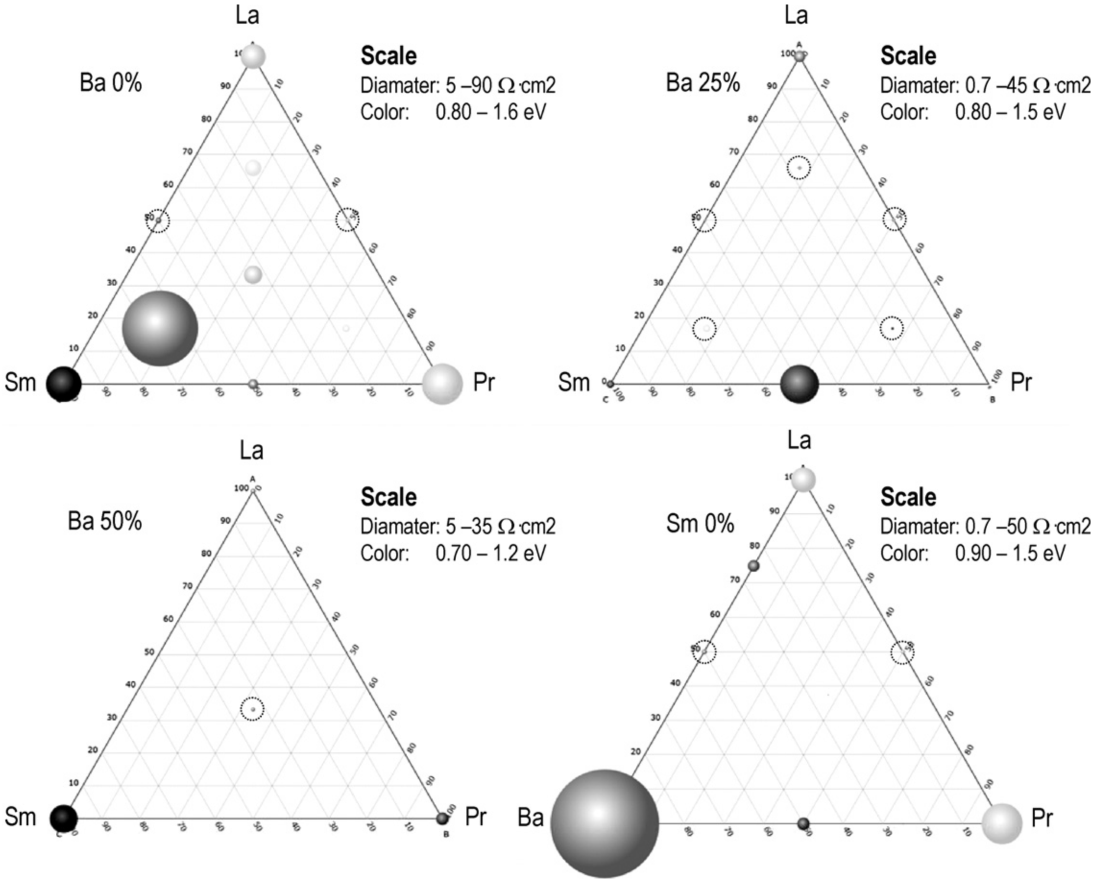

Fig. 8. Electrochemical results derived from equivalent circuit analysis as a function of the operating temperature and sample composition. Polarization resistance at 500 °C (bubble diameter) and activation energy in the range 450–650 °C (bubble color) are represented in the corresponding ternary sections of the whole quaternary design. Dot circles remark the presence of an experimental point with small resistance or activation energy.

jected to a discrete number of dimensions by applying different data mining techniques: (i) clustering analysis using K-means; and (ii) principal component analysis (PCA). The raw XRD data was normalized in intensity considering the most intense diffraction peak and PCA was performed directly on the normalized raw spectra matrix. Due to the systematic XRD analysis it was neither necessary to produce a similarity matrix nor to center it.

Fig. 4 shows the complete spectral data ordered with increasing unit cell dimension. Fig. 4a shows the whole spectral dataset (20°–90° diffraction range) in two different projections, i.e., merged XRD patterns (top) and contour plot (bottom) on the sample vs. diffraction plane. Fig. 4b shows the similar graphs for a selected angle range, in where details of the most intense diffraction peak and the occurrence of secondary symmetry diffractions can be observed. Fig. 5 presents the distribution of the experimental data points in the PCA space (three-dimensional) and the use of K-means clustering algorithm is used to illustrate the diversity across this space. Specifically, Fig. 5 shows the cluster distribution obtained using K-means algorithm, when plotted using as coordinates the principal components obtained by PCA computation. The results show that apparently the clusters found are clearly separated one to each other, when displayed using the PCA projection.

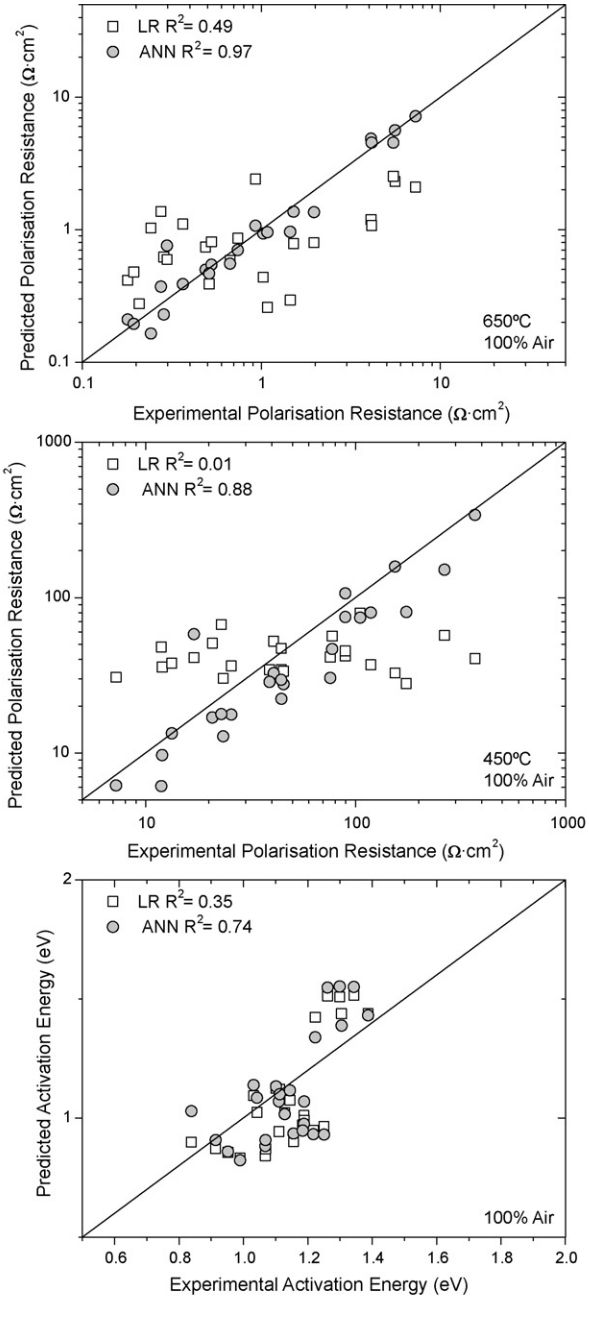

Fig. 9. Electrochemical descriptors modeling using compositional data as input. Parity plots for the polarization resistance at 650 and 450 °C and activation energy using linear regression and ANNs. The best ANN model for each parameter is 3-4-2-1 (R_p 650 °C), 3-7-2-1 (R_p 450 °C) and 3-4-2-1 (activation energy 650 °C). Note the logarithmic scale for the polarization resistance (top and middle charts).

After PCA computation using the whole available dataset, the XRD data was reduced to a vector with only three to five descriptors and the percentage of variance for the first principal components is 20.0%, 12.9% and 13.0%, respectively. These simplified spectral descriptors provide an easy visualization of the distribution of the samples into the virtual three-dimensional *structural* space although rationalization of these components is not straightforward [39]. In fact, XRD data usually contains information about the type of crystalline phase as well as about the lattice parameters, crystallite size, crystalline phase distribution, etc. Consequently, these new structural descriptors contain the summarized information of XRD patterns describing the different structural and morphological changes in the whole of explored materials [24]. This information should be redundant with the parameters obtained by knowledge-guided analysis although the unsupervised (PC) descriptors may contain unexpected structural features that are skipped in the previous analysis based on human experience.

The PC vectors were modeled using the material composition as model input. Firstly, a linear regression was obtained for each individual principal component. The regression coefficient for PC1 and PC2 was 0.735 and 0.697 and these values are in line with those obtained by the linear regression of the lattice parameter (a'). On the other hand, the regression coefficient for PC3 was very poor and this can be due to (i) high non-linearity with regard to composition variables or (ii) low PC significance. The three principal components were subsequently modeled using neural networks. The best ANN model has a simple topology 3-3-3 and the relative input significance follows the order 0.575 (Ba), 0.330 (La) and 0.235 (Pr). This order is similar to that observed for the ANN modeling of the lattice parameter and the steps between input variable significance are also similar (see Figs. 2 and 6). The prediction performance was improved substantially for all three components although the major improvement was achieved for the PC3. In principle, PC3 seems to be a relevant structural feature with a notable non-linearity with respect to the material composition. For the given design, it is possible to find accurate relationships between the structural descriptors derived from unsupervised treatment of XRD spectra and the nominal lattice composition.

5. Analysis of impedance spectroscopy spectra and quantitative composition/structure–activity relationships

Raw impedance spectroscopy spectra have been corrected by subtracting the inductive tail and the ohmic electrolyte contribution. Fig. 7 shows an example of corrected spectra in a Nyquist representation (imaginary impedance (Z'') versus real impedance (Z') values). Two arcs can be distinguished although these arcs appear more overlapped. The equivalent circuit model is shown in Fig. 7, which consists of the set-up inductance, electrolyte resistance and two arcs. The higher frequency arc is a depressed semicircle which can be modeled as a parallel combination of a resistor with a constant phase element (designated as CPE or Q) described by:

$$Z_{\mathrm{CPE}} = \frac{1}{Q_0 \cdot (j\omega)^n} \quad (1)$$

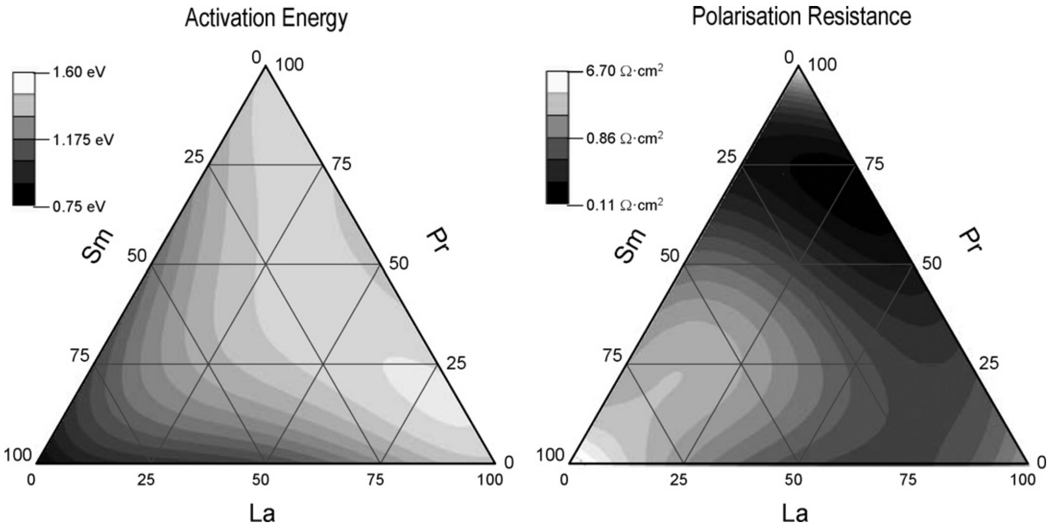

Fig. 10. Compositional mapping simulated from best ANN models for (left-hand) activation energy and (right-hand) polarization resistance at 650 °C for the Ba-free plane. Note the log scale in the resistance scale bar.

where Q_0 can be compared to a capacitance value but with $\mathrm{F\,s}^{n-1}$ ($\mathrm{S\,s}^n$) units, and n being the frequency exponent, indicating the degree of depression of the semicircle. The low frequency arc can be modeled as a Gerischer element, which mathematical formula is described by:

$$Z_G = \frac{Z_0}{\sqrt{k + j\omega}} \quad (2)$$

where Z_0 is a resistance-like parameter with $\Omega\,\mathrm{s}^{-0.5}$ units and k is a reaction rate constant [40] in s^{-1}. This reaction rate constant (k) is an indicator of the limiting process of the oxygen reduction reaction on mixed ionic-electronic conductors where a competition between bulk and surface diffusion take place at same time.

An appropriate figure of merit for these catalytic layers is the sum of the real resistance value corresponding to both arcs. This value corresponds to the polarization resistance (R_p) and it can be computed for the whole range of temperatures. R_p followed an Arrhenius behavior and therefore it can be calculated the activation energy for each compound. Fig. 8 shows an illustration of the data extracted from this analysis, i.e., activation energy (bubble color) and polarization resistance (bubble diameter) obtained at 500 °C and under undiluted airflow. It can be observed that high-performing materials with low polarization resistance could be identified within the experimental chosen space. It was possible to identify electrode compositions combining both low polarization resistance and low activation energy and the best formulations are ternary compounds (La–Pr–Ba, La–Sm–Ba and La–Pr–Sm), which join the best catalytic/conduction properties of the selected single elements. The most promising compositions in terms of polarization resistance and oxygen activation are $La_{0.2175}Pr_{0.2175}Ba_{0.145}Sr_{0.4}Fe_{0.8}Co_{0.2}O_{3-\delta}$ and $Pr_{0.435}Ba_{0.145}Sr_{0.4}Fe_{0.8}Co_{0.2}O_{3-\delta}$.

5.1. Quantitative composition–activity relationships

Fig. 9 presents the modeling results for the three selected electrochemical descriptors: polarization resistance (R_p) at 650 and 450 °C and activation energy. In the experimental space chosen, the polarization resistance varies up to two orders of magnitude and therefore a logarithmic scale (transformation) was applied for modeling and visualization purposes. The linear regression shows very poor results (see figure legend) while the best fitted ANN can model properly the electrochemical descriptors. R_p at 650 °C is particularly well modeled ($R^2 = 0.97$) and the relative significance of the input variables is 0.69 (Ba), 0.55 (La) and 0.48 (Pr). The achieved prediction performance is high, especially considering the experimental error contained in the impedance experimental data. Slightly less accurate predictions ($R^2 = 0.88$) are obtained for R_p at 450 °C while the input variable significance is quite similar, i.e., 0.61 (Ba), La

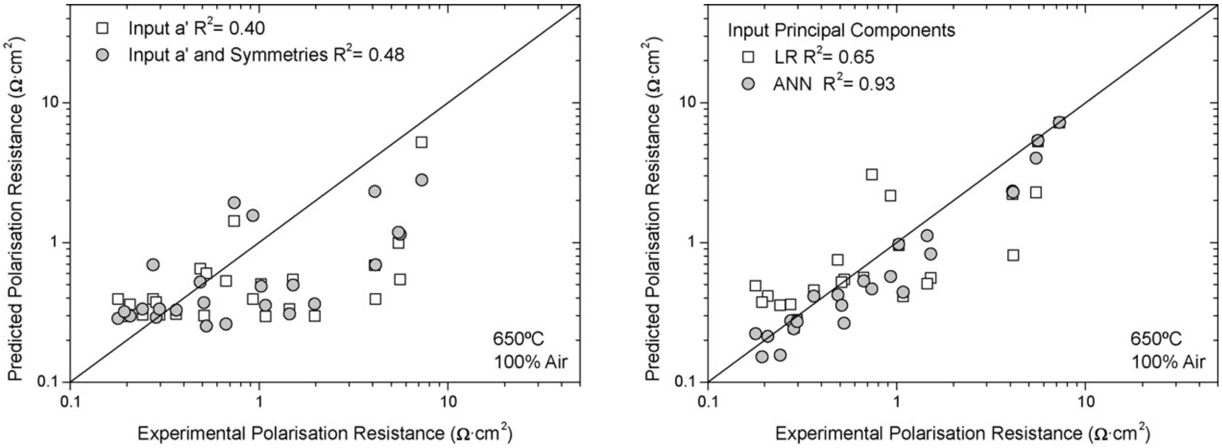

Fig. 11. Electrochemical descriptors modeling using structural data as input. Parity plots for the polarization resistance at 650 °C using (left-hand) knowledge-based structural parameters using ANN (both ANN have a topology using only 3 neurons in a single hidden layer) and (right-hand) XRD data principal components as input variables.

(0.51) and 0.44 (Pr). On the other hand, the prediction performance for the activation energy is less accurate and the model principally allows distinguishing the class of activation energy (high level for Ba-free materials and low level for Ba-containing ones). See bottom chart in Fig. 9. In this case, the relative significance of the input variables is Ba (0.66), Pr (0.52) and La (0.40). Fig. 10 shows a simulated mapping for a specific composition plane (Ba-free). This picture illustrates how the built models allow visualizing the experimental space and how new candidates for further optimization could be suggested. Finally, it was proved that the simultaneous ANN modeling of different EIS-derived variables did not result in the improvement of the prediction capacity.

5.2. Quantitative structure–activity relationships

Fig. 11 summarizes the modeling of the polarization resistance at 650 °C using as input three sets of descriptors: (1) uniquely the lattice parameter; (2) lattice parameter and the relative abundance of orthorhombic and hexagonal symmetry; (3) the five computed principal components derived from the analysis of XRD data. The ANN prediction performance obtained using the descriptors set (1) and (2) – see left-hand chart in Fig. 11 – is poor and it is only possible to obtain a rough estimation of the material activity by using lattice parameter and symmetry information as input variable. In contrast, the use of the principal components as input variable makes possible to achieve acceptable prediction performance. It was achieved a regression coefficient (R^2) of 0.93 by using a quite simple neural network topology (5-3-1). The relative significance of the principal components was 0.71 (PC1), 0.69 (PC2), 0.53 (PC4) and 0.38 (PC3 and PC5). Consequently, a quantitative structure–property relationship has been constructed and would allow predicting the material performance within the explored experimental space when a new XRD pattern is available. The concrete meaning of the principal components and the reason of the correlation with the electrochemical performances deserve future investigations. On the other hand, the deviation of predicted values from the experimental data is not negligible and this might be related to the influence of other variables on the electrode performance apart from compositional and lattice parameters. These variables include for instance changes in the layer microstructure due to (i) the compositional variation; (ii) deviations while manufacturing and sintering, thickness, and (iii) in some cases due to the possible chemical reaction or interdiffusion between the cathode and the electrolyte [41,42].

6. Conclusions

Experimental data derived from the optimization of oxygen electrocatalysts based on the perovskite $Ln_{0.58}Sr_{0.4}Fe_{0.8}Co_{0.2}O_{3-\delta}$ system ($Ln = La_{1-x-y-z}Pr_xSm_yBa_z$) have been modeled following different approaches. The experimental datasets available for the series of materials can be divided into: composition data, structural data (X-ray diffraction patterns), and electrochemical characterization data (electrochemical impedance spectra). Dimensional reduction of powder X-ray diffraction data was conducted by using principal components analysis, clustering, whilst predictive models were obtained using linear regression and artificial neural networks. Quantitative compositions–structure relationships and composition–property relationships have been successfully built, achieving a high prediction performance for some specific relationships. Moreover, quantitative structure–property relationships have been constructed for the prediction of the polarization resistance and this model would allow predicting the material performance within the explored experimental space when a new XRD pattern is available.

Acknowledgements

Funding from Universitat Politècnica de València (grant UPV-2007-06), the Spanish Ministry for Science and Innovation (Project ENE-2008-06302), the Helmholtz Association of German Research Centers through the Helmholtz Alliance MEM-BRAIN (Initiative and Networking Fund) and EU through FP7 NASA-OTM Project (NMP3-SL-2009-228701) is kindly acknowledged.

Appendix A. Supplementary data

Supplementary data associated with this article can be found, in the online version, at doi:10.1016/j.cattod.2010.06.019.

References

[1] S. Tedmon Jr., H.S. Spacil, S.P. Mitoff, J. Electrochem. Soc. 116 (1969) 1170.
[2] A. Esquirol, N.P. Brandon, J.A. Kilner, M. Mogensen, J. Electrochem. Soc. 151 (2004) A1847–A1855.
[3] A. Mai, V.A.C. Haanappel, S. Uhlenbruck, F. Tietz, D. Stöver, Solid State Ionics 176 (2005) 1341–1350.
[4] J.M. Serra, H.-P. Buchkremer, J. Power Sources 172 (2007) 768–774.
[5] M.A. Peña, J.L. Fierro, Chem. Rev. 1001 (7) (2001) 1981–2017.
[6] H.M. Reichenbach, P.J. McGinn, Appl. Catal. A 244 (1) (2003) 101–114.
[7] Y. Song, J. Yu, G. Li, Y. Li, Y. Wang, R. Xu, Chem. Commun. (2002) 1720–1721.
[8] R. Wendelbo, D.E. Akporiaye, A. Karlsson, M. Plassen, A. Olafsen, J. Eur. Ceram. Soc. 26 (2006) 849–859.
[9] H. Wang, Z. Liu, J. Shen, H. Liu, Catal. Commun. 5 (2004) 55–58.
[10] C. Kiener, M. Kurtz, H. Wilmer, C. Hoffmann, H.-W. Schmidt, J.-D. Grunwaldt, M. Muhler, F. Schuth, J. Catal. 216 (2003) 110–119.
[11] H. Wang, Z. Liu, J. Shen, H. Liu, Catal. Commun. 5 (2004) 55–58.
[12] P. Atienzar, A. Corma, H. García, J.M. Serra, Chem. Eur. J. 10 (2004) 6043–6047.
[13] B.E. Baker, N.J. Kline, P.J. Treado, M.J.J. Natan, J. Am. Chem. Soc. 118 (1996) 8721.
[14] A. Frantzen, J. Scheidtmann, G. Frenzer, W.E. Maier, J. Jockel, T. Brinz, D. Sanders, U. Simon, Angew. Chem. Int. Ed. 43 (6) (2004) 752–754.
[15] J.-D. Grunwaldt, B. Kimmerle, S. Hannemann, A. Baiker, P. Boye, C.G. Schroer, J. Mater. Chem. 17 (2007) 2063–2606.
[16] L.A. Baumes, M. Moliner, N. Nicoloyannis, A. Corma, CrystEngcomm. 10 (10) (2008) 1321–1324.
[17] G. Barr, W. Dong, C.J. Gilmore, J. Appl. Crystallogr. 42 (5) (2009) 965–974.
[18] G.A. Landrum, H. Genin, J. Solid State Chem. 176 (2003) 587–593.
[19] C. Suh, K. Rajan, QSAR Comb. Sci. 24 (2005) 114–119.
[20] J.M. Serra, A. Corma, S. Valero, E. Argente, V. Botti, QSAR Comb. Sci. 26 (2007) 11–26.
[21] L.A. Baumes, D. Farruseng, M. Lengliz, C. Mirodatos, QSAR Comb. Sci. vol. 29 (9) (2004) 767–778.
[22] A. Corma, J.M. Serra, E. Argente, S. Valero, V. Botti, ChemPhysChem 3 (2002) 939–945.
[23] L.A. Baumes, J.M. Serra, P. Serna, A. Corma, J. Comb. Chem. 8 (4) (2006) 583–596.
[24] A. Corma, J.M. Serra, P. Serna, M. Moliner, J. Catal. 232 (2005) 335–441.
[25] D. Farrusseng, Surf. Sci. Rep. 63 (11) (2008) 487–513.
[26] A. Corma, J.M. Serra, Catal. Today 107–108 (2005) 3–11.
[27] W.F. Maier, K. Store, S. Sieg, Angew. Chem. Int. Ed. 46 (32) (2007) 6016–6067.
[28] E. Reddington, A. Sapienza, B. Gurau, R. Viswanathan, S. Sarangapani, E.S. Smotkin, T.E. Mallouk, Science 280 (5370) (1998) 1735–1737.
[29] J.M. Serra, V.B. Vert, ChemSusChem 2 (10) (2009) 957–961.
[30] J.M. Serra, V.B. Vert, M. Betz, V.A.C. Haanappel, W.A. Meulenberg, F. Tietz, J. Electrochem. Soc. 155 (2008) B207.
[31] J.M. Serra, S. Uhlenbruck, W.A. Meulenberg, H.P. Buchkremer, D. Stöver, Top. Catal. 40 (1–4) (2006) 123–131.
[32] M. Siemons, T. Weirich, J. Maier, U. Simon, Zeitschrift Anorgan. Allgem. Chem. 630 (12) (2004) 2083–2089.
[33] S.B. Adler, J.A. Lane, B.C.H. Steele, J. Electrochem. Soc. 143 (1996) 3554.
[34] V.B. Vert, J.M. Serra, Fuel Cells 5 (2009) 663.
[35] Clementine® 9.0 Desktop User's Guide, SPSS Inc., Chicago, 2000.
[36] L.A. Baumes, S. Jimenez, A. Corma, hITeQ: A new workflow-based computing environment for streamlining discovery. Application in materials science, Catal. Today 159 (2011) 126–137.
[37] N. Dasgupta, R. Krishnamoorthy, K. Thomas Jacob, Mater. Sci. Eng. B 90 (2002) 278.
[38] PANalytical B.V., X'Pert HighScore Plus software, Version 2.2b, Almelo, The Netherlands, 2006.
[39] A. Corma, M. Moliner, J.M. Serra, P. Serna, M.A. Diaz-Cabañas, L.A. Baumes, Chem. Mater. 18 (2006) 3287–3296.
[40] M. Sluyters-Rehbach, J.H. Sluyters, Comprehensive treatise of electrochemistry Electrodiscs: Experimental Techniques, vol. 9, Plenum, New York, 1984.
[41] A. Mitterdorfer, L.J. Gauckler, Solid State Ionics 111 (3–4) (1998) 158.
[42] K. Wang, R. Ran, W. Zhou, H. Gu, Z. Shao, J. Ahn, J. Power Sources 179 (2008) 60–68.